Thermoelectric properties of double-substituted tetrahedrites Cu12–xCoxSb4–yTeyS13

Yohan Bouyrie, Selma Sassi, Christophe Candolfi, Jean-Baptiste Vaney, Anne Dauscher, Bertrand Lenoir

Thermoelectric properties of double-substituted tetrahedrites $Cu_{12-x}Co_xSb_{4-y}Te_yS_{13}$

Y. Bouyrie[1], S. Sassi, C. Candolfi[*], J.-B. Vaney, A. Dauscher and B. Lenoir

Institut Jean Lamour, UMR 7198 CNRS – Université de Lorraine, Parc de Saurupt, CS 50840, 54011 Nancy, France

[*]Corresponding author: christophe.candolfi@univ-lorraine.fr

[1] Present address: Present address: National Institute of Advanced Industrial Science and Technology, AIST Tsukuba Central 2, Umezono 1-1-1, Tsukuba, Ibaraki, 305-8586, Japan. bouyrie.yohan@aist.go.jp

Abstract

Tetrahedrites, a class of earth-abundant minerals, exhibit extremely low thermal conductivity values making them promising candidates for thermoelectric applications at high temperatures. Herein, we extend investigations on these materials to specimens substituted on both the Cu and Sb sites by reporting on the thermoelectric properties of polycrystalline $Cu_{12-x}Co_xSb_{4-y}Te_yS_{13}$ in a wide range of temperatures (2 – 700 K). All prepared samples exhibit *p*-type heavily-doped semiconducting behavior with relatively low electrical resistivity values. These substitutions have little influence on the thermal conductivity, which remains very low in the whole temperature range (~ 0.7 W m^{-1} K^{-1}). Although the double-substituted samples exhibit higher *ZT* values with respect to the parent tetrahedrite $Cu_{12}Sb_4S_{13}$, the maximum *ZT* of 0.80 reached at 700 K for (*x*,*y*) = (0.82, 0.41) remains comparable to the values obtained in compounds solely substituted with Co or Te.

Introduction

Thermoelectric generators enable converting directly heat into electricity and vice-versa, making them an environmentally-friendly way to harvest waste heat into useful electric power.[1,2] The performances of thermoelectric materials are determined by the dimensionless thermoelectric figure of merit $ZT = \alpha^2 T / \rho\kappa$, where T is the absolute temperature, α is the Seebeck coefficient or thermopower, ρ is the electrical resistivity, and κ is the total thermal conductivity.[1,2] To achieve high ZT values in order to maximize the conversion efficiency, materials exhibiting an unusual combination of low thermal conductivity, low electrical resistivity, and high thermopower are intensively sought.[3,4] However, the interdependence of these three transport coefficients provides a difficult challenge to overcome.

Due to their complex crystal structures, rich chemistry and tunable transport properties, copper sulfosalts are receiving increasing attention. Several families of minerals such as colusite $Cu_{26}V_2M_6S_{32}$ (M = Ge or Sn), bornite Cu_5FeS_4 or $Cu_4Sn_7S_{16}$ show naturally extremely low thermal conductivity, typically well below 1 W m^{-1} K^{-1} above room temperature.[5-9] Tetrahedrites are also currently under scrutiny due to their abundance on Earth and interesting transport properties.[10,11] This class of minerals has a general chemical formula that can be written as $A_{10}B_2X_4Y_{13}$, with A = Cu or Ag, B = transition metals such as Fe, Ni, Zn, Mn or Co, X = Sb, As or Te, and Y = S that can be partially substituted by Se. They crystallize into a body-centred cubic structure (space group $I\bar{4}3m$) with 58 atoms per unit cell. These minerals are composed of relatively earth-abundant elements and show a large variety of substitutions, which provide several degrees of freedom to optimize the power factor α^2 / ρ as demonstrated in recent studies on synthetic tetrahedrites $Cu_{12-x}B_xSb_4S_{13}$ (Ref. 10-20) and $Cu_{12}Sb_{4-y}Te_yS_{13}$.[21,22] When properly optimized, maximum ZT values near unity are achieved around 700 K.[10,22] These high ZT values arise from the beneficial combination of

semiconducting properties and very low lattice thermal conductivity. The poor ability of tetrahedrites to transport heat has been recently shown to originate from the interaction between active lone-pair electrons on the Sb atoms and neighbouring Cu atoms.[17,20] Inelastic neutron scattering experiments carried out on both single-crystalline and polycrystalline samples have demonstrated the presence of a strongly anharmonic, low-energy excess of vibrational states related to the off-plane thermal vibrations of these Cu atoms.[17] The strong coupling between these optical modes and acoustic phonons efficiently lowers the lattice thermal conductivity and explains its glass-like temperature dependence below room temperature.[17]

With very few exceptions, prior studies have so far mainly focused on a single substitution on either the Cu or Sb site. Lu *et al*.[23] recently reported the beneficial influence of Zn on the thermoelectric properties of Ni-substituted $Cu_{12}Sb_4S_{13}$ suggesting that double substitutions are a promising strategy for further enhancing the *ZT* values. Yet, the influence of double substitutions on both the Cu and Sb site remains only scarcely explored.[24] Among the various elements that substitute on Cu and alter the thermoelectric properties of $Cu_{12}Sb_4S_{13}$, the choice of Co resulted in a significant enhancement of the *ZT* values up to 0.98 at 673 K in $Cu_{11.5}Co_{0.5}Sb_4S_{13}$ *i.e.* one of the highest reported value for a single aliovalent substitution on the Cu site.[19] The possibility to further manipulate the thermoelectric properties upon Te substitution in this particular system is thus enticing. For this reason, we report herein on a systematic investigation of the influence of Te insertion on the crystal structure, chemical homogeneity and transport properties in a broad range of temperatures (2 – 700 K) of synthetic tetrahedrites $Cu_{12-x}Co_xSb_4S_{13}$.

Experimental section

Synthesis

Two series of polycrystalline samples, $Cu_{12-x}Co_xSb_4S_{13}$ with x = 1.00, 1.25, 1.50 and 1.75 and $Cu_{12-x}Co_xSb_{4-y}Te_yS_{13}$ with (x,y) = (0.50, 0.50), (0.50, 0.75), (0.50, 1.0) and (1.0, 0.5), were synthesized by a conventional powder metallurgy route. All manipulations were carried out under controlled atmosphere in a dry, argon-filled glove box. High-purity elemental powders (Cu, 99.99 %, Co, 99.99%, Sb, 99.999 %, Te, 99.999 % and S, 99.999 %) were weighted in stoichiometric amounts and placed in evacuated quartz tubes, systematically preheated at 1173 K for several hours under dynamic vacuum to ensure dry conditions. The sealed ampules were then heated to 923 K at 0.3 K min^{-1}, and subsequently maintained at this temperature for 12h. In a final step, the tubes were cooled down to room temperature at a rate of 0.4 K min^{-1}. Such low heating and cooling rates were applied in order to avoid an excessive sulfur vapor pressure inside the ampules. The obtained ingots were crushed into fine powders, cold-pressed into cylindrical pellets and further annealed at 673 K for at least one week in evacuated quartz tubes. In a final step, the annealed pellets were ground into fine powders and consolidated in graphite dies by spark plasma sintering (SPS) at 723 K under 80 MPa for 12 min. For both series, the relative density of the samples, determined by weight and sample dimensions, was above 92% of the theoretical density.

Structural and chemical characterizations

The chemical compositions of the samples were determined by energy and wavelength dispersive X-ray spectroscopy (EDXS/WDXS) using a JEOL J7600F instrument. $CuFeS_2$,

ZnS, Co, Sb, Te were used as standards to measure the Cu, S, Co, Sb and Te concentrations, respectively. In average, 15 spots measured on the surface of each samples were collected. The actual chemical compositions, listed in Table 1, were obtained by normalizing the S contents to 13 sulfur atoms. Hereafter, the actual Co and Co-Te contents will be used to label the samples of each series.

Phase purity and elemental mappings were conducted by powder X-ray diffraction (PXRD) and scanning electron microscopy (SEM). Phase purity of the samples was assessed by PXRD with a Bruker D8 Advance diffractometer using CuKα_1 radiation (λ = 1.54056 Å). The room-temperature lattice parameters were determined by Rietveld refinements using the Fullprof software (Ref. 25) and are listed in Table 2. The chemical homogeneity of the samples was verified by SEM experiments using a Quanta FEG (FEI). In order to contrast impurity phases from the tetrahedrite phase, images of the sample's surface were collected in backscattered electron mode (BSE). The spatial distribution of the elements was determined by elemental X-ray mapping.

Transport properties measurements

Thermopower, electrical resistivity and thermal conductivity were measured simultaneously between 5 and 300 K using the thermal transport option (TTO) of a physical property measurement system (PPMS, Quantum Design). For these measurements, bar-shaped samples with typical dimensions of 2.5×2.5×8 mm^3 were cut with a diamond-wire saw from the consolidated pellets. The electrical and thermal contacts on the samples were realized by attaching four copper leads with a silver epoxy. Thermopower and electrical resistivity were measured simultaneously between 300 and 700 K with a ZEM-3 system (Ulvac-Riko) on bar-shaped samples of similar dimensions. The thermal conductivity κ was determined at high

temperatures (300 – 700 K) by measuring the thermal diffusivity *a* by a laser flash technique (LFA 427, Netzsch). The thermal conductivity was then calculated from the relation $\kappa = aC_p d$ where *d* is the experimental density of the sample whose temperature dependence has been neglected in the present case. The specific heat was assumed to be equal to the temperature-independent Dulong-Petit value above 300 K. A good agreement between the low and high-temperature data sets was observed at room temperature, the largest discrepancy being visible on the thermal conductivity. This measurement is inevitably accompanied by thermal radiations below 300 K, specifically in samples exhibiting a low thermal conductance. The combined experimental uncertainty in *ZT* is estimated to be 17%.[26]

Results and discussion

Structural and chemical characterizations

To better understand the influence of Te on the crystallographic and transport properties of the tetrahedrites $Cu_{12-x}Co_xSb_4S_{13}$, we prepared and characterized in a first step a series of Te-free samples. The number of possible compositions being very large when considering double substitutions, we restricted our study to a limited range of Co and Te concentrations. Our choices have been dictated by the results reported by Chetty *et al.*[19] who showed that the optimum *ZT* values in $Cu_{12-x}Co_xSb_4S_{13}$ are achieved near $x = 0.5$. We have therefore prepared several samples trying to keep constant the Co content to $x = 0.5$ while progressively increasing the Te concentration from $y = 0.50$ up to $y = 1.0$. An additional sample with a nominal composition $(x,y) = (1.0, 0.50)$ has also been synthesized for comparison with the $(x,y) = (0.50, 1.0)$ sample in order to gain some insights into the influence of the Co/Te ratio on the thermoelectric properties.

Figures 1a and 1b show representative PXRD patterns with their Rietveld refinements obtained for the illustrative x = 1.70 and (x,y) = (0.25, 0.62) samples, respectively. For both series, all the PXRD data could be successfully refined within the $I\bar{4}3m$ space group of tetrahedrite. Except for the x = 1.70 sample, which presents a small fraction (3% vol.) of impurity identified as $CuSbS_2$, all samples of the Co series are single-phase based on PXRD. The same conclusion holds for the samples of the Co-Te series for which, only the (x,y) = (0.32, 1.05) specimen shows the same impurity.

According to BSE and elemental X-ray mapping images, all the elements are homogeneously distributed within the tetrahedrite phase (Figure 2a). These experiments also revealed the presence of minute amount of CoS_2 in addition to $CuSbS_2$ in the samples of the Co series (Figure 2b). The addition of Te yield homogeneous specimens regardless of the Co-to-Te ratio (Figure 3) with only traces of CoS_2 and $CuSbS_2$ as secondary phases.

The room-temperature lattice parameters are shown in Figures 4a and 4b as a function of the actual Co content and the sum of the actual Co and Te concentrations, respectively. For both series of samples, a is larger than that of the ternary compound $Cu_{12}Sb_4S_{13}$ indicative of the successful insertion of Co or Co-Te in the crystal structure. In the Co series, a increases quasi-linearly with the Co content following a Vegard's law (Figure 4a), in agreement with the results of Chetty *et al.*[19] When both Co and Te are present, a trends with the sum of the actual Co and Te concentrations, both of which tending to expand the unit cell.[10,19,21,22] The values obtained are in excellent agreement with those expected when considering a linear variation of a with x and y and the actual Co and Te contents (Table 2). The fact that no anomaly is seen in the dependence of a with x is in contrast to what was seen in Te-substituted samples prepared from precursor compounds for which, very large lattice parameters at low Te contents have been obtained.[21] Hence, the conventional behavior of a in

the present series of samples suggests the absence of off-stoichiometry in their chemical compositions.

The chemical compositions measured by EDXS/WDXS for all the $Cu_{12-x}Co_xSb_{4-y}Te_yS_{13}$ samples (Table 1) show a very good correlation between nominal and actual compositions for the Co series, except for the $x = 0.90$ sample that seems to show an excess of Cu. This holds true for the Co-Te series where the actual Cu content seems to deviate significantly only in the $(x,y) = (0.25, 0.62)$ sample. Several studies have demonstrated that tetrahedrites are prone to significant deviations from stoichiometry in contrast to natural tetrahedrites, which are more stoichiometric.[27] This phenomenon seems even more pronounced than the level of substitution decreases *i.e.* when the composition tends to $Cu_{12}Sb_4S_{13}$, a ternary compound well-known to show deviations from stoichiometry and to undergo an exsolution process below 403 K.[28-31] However, the presence of off-stoichiometry is correlated to large lattice parameters, as recently shown in the $Cu_{12}Sb_{4-y}Te_yS_{13}$ tetrahedrites. Neither the $x = 0.9$ sample nor the $(x,y) = (0.25, 0.62)$ specimen exhibit abnormal a values indicating that these deviations are most likely due to the experimental uncertainty.

For the Co-Te series, we note that the actual Te content nearly matches the nominal value while the Co concentration deviates more significantly. The more pronounced off-stoichiometry in Co in the $Cu_{12-x}Co_xSb_{4-y}Te_yS_{13}$ samples compared to the $Cu_{12-x}Co_xSb_{4-y}S_{13}$ series suggests a competition between the insertion of Co and Te that results in lower Co concentrations in the actual composition when both elements are present. This finding is consistent with a recent study on the $Cu_{12-x}Zn_xSb_{4-y}Te_yS_{13}$ and $Cu_{12-x}Ni_xSb_{4-y}Te_yS_{13}$ tetrahedrites, for which a similar tendency has been underlined.[24]

Transport properties

The temperature dependence of the electrical resistivity is shown in Figures 5a and 5b for the Co and Co-Te series, respectively. From simple electron counting rules, both substitutions should provide additional electrons driving the system from a *p*-type metallic state observed in $Cu_{12}Sb_4S_{13}$ towards a semiconducting behavior that develops when two electrons per formula unit are added (*i.e.* when $x = 2$ or $x + y = 2$). Hence, an increase in ρ with increasing the concentration of the substituents can be anticipated as observed in prior studies on tetrahedrites.[10-16,19,21-24] The data collected for both series are consistent with these expectations and show that ρ increases with x or with the sum $x + y$. Since the concentrations of Co and Co-Te are lower than the limit required to reach a semiconducting state, all samples behave as heavily-doped semiconductors characterized by a smooth increase in ρ with temperature above 300 K. Interestingly, while a monotonic decrease in the ρ values upon cooling would be expected, ρ significantly increases below 100 K for all samples. In the Co series, this low-temperature behavior trends with the Co content, the rise in the ρ values reaching several orders of magnitude in the $x = 1.51$ and 1.70 samples. This sharp increase in ρ suggests that the hole mobility significantly decreases upon cooling, the hole concentration being usually nearly constant with temperature in heavily-doped semiconductors. As mentioned by Lu *et al.*[11] and in our prior study (Ref. 21), Hall effect measurements, that would be necessary to ascertain this picture, are difficult to perform on tetrahedrites due to a nearly null Hall signal. An exsolution process resulting in the coexistence of two tetrahedrite phases can be ruled out in the present case since none of the transport properties exhibit an anomaly as recently seen below 300 K in Te-substituted tetrahedrites.[32] As noted by Lu *et al.*[11], the ρ(T) data does not follow a simple activated behavior expected in a semiconducting state, rather suggesting that the electrical conduction enters a hopping-like regime below ~

100 K.

Figures 6a and 6b shows the temperature dependence of the thermopower. In agreement with the *p*-type character of the parent compound $Cu_{12}Sb_4S_{13}$, all the samples exhibit positive α values. Regardless of the composition, α monotonically increases with temperature to reach values ranging between 150 and 240 μV K^{-1} at 673 K. For both series, the observed increase in α with increasing the concentration of Co or Co-Te is consistent with a gradual evolution towards a semiconducting state.

The temperature dependence of the total thermal conductivity for the Co and Co-Te series is shown in Figures 7a and 7b, respectively. Regardless of the composition, the κ values are extremely low, ranging between 0.5 and 0.9 W m^{-1} K^{-1} above 300 K. Below this temperature, none of the samples show a dielectric maximum, mimicking an amorphous-like behavior. Inelastic neutron scattering measurements have shown that the suppression of this peak originates from an additional Umklapp scattering channel due to the low-lying dispersionless optical branch associated to the out-of-plane thermal motion of the Cu atoms in their triangular chemical environment.[17] The fact that all Co and Co-Te samples share a similar temperature dependence further demonstrates that this low-energy optical branch is insensitive to the site on which the aliovalent substitution is made.

Due to the more pronounced metallic character of the samples in the Co-Te series, the electronic contribution to the thermal conductivity κ_e is higher in these samples than in the Co analogues. To disentangle the lattice and the electronic contribution to κ, the latter has been estimated by using the Wiedemann-Franz law $\kappa_e = LT/\rho$ where L is the Lorenz number. Below 300 K, the temperature dependence of L has been neglected and the room-temperature values were used to estimate κ_e. The temperature dependence of L above 300 K has been determined by using a single-parabolic band model and assuming that acoustic phonon scattering is the dominant source of diffusion of the charge carriers.[19] This model led

to L values ranging between 1.7 – 1.8×10^{-8} V^2 K^{-2} and 1.8 – 1.9×10^{-8} V^2 K^{-2} at 300 K for the Co and Co-Te series, respectively. The former are in excellent agreement with those inferred by Chetty *et al.*[19] in Co-substituted tetrahedrites with similar compositions. As shown in Figures 7c and 7d, the lattice thermal conductivity $\kappa_L = \kappa - \kappa_e$ is nearly independent of the composition and is of the order of 0.4 to 0.5 W m^{-1} K^{-1} at high temperatures, which further show that these compounds can be classified among the best thermal insulators reported so far.[33-40] Above 300 K, these values approach the minimum lattice thermal conductivity estimated to 0.45 W m^{-1} K^{-1} using the model developed by Cahill *et al.*[41]

From the combination of the electronic and thermal transport data, the temperature dependence of *ZT* was determined for each sample (Figures 8a and 8b). Peak *ZT* values of 0.75 and 0.80 are obtained at 673 K for x = 0.90 and (x,y) = (0.82, 0.41). Despite a clear enhancement of the *ZT* values with respect to the parent compound (0.56 at 673 K), this double substitution does not further enhance the thermoelectric performances of tetrahedrites solely substituted with either Co or Te.[19,21,22] The data obtained on the Co-Te series are similar to those achieved in the $Cu_{12-x}M_xSb_{4-y}Te_yS_{13}$ (with M = Ni, Zn) compounds,[24] suggesting that co-substitution on both the Cu and Sb sites does not enable to further improve the *ZT* values with respect to optimized quaternary tetrahedrites. Yet, the fact that the highest *ZT* values in the double-substituted samples are achieved for $y > x$ tends to indicate that the concentration of Te should remain low to achieve high *ZT*.

Conclusion

We reported on the synthesis of two series of $Cu_{12-x}Co_xSb_{4-y}Te_yS_{13}$ tetrahedrites by direct melting of pure elements at high temperature followed by SPS sintering. PXRD and SEM analyses revealed the presence of small amount of secondary phases identified as CoS_2 and

$CuSbS_2$. EDXS/WDXS experiments indicated a systematic deviation from the nominal Co concentration in the co-substituted series suggesting a competition between transition metals and Te in tetrahedrites. All the compositions studied show trends typical of heavily-doped semiconductors with relatively low electrical resistivity and high thermopower values. The concentration of Co and/or Te does not influence markedly the thermal conductivity, which remains very low in the whole temperature range investigated. Although a peak *ZT* of 0.80 at 673 K has been achieved for the composition (x,y) = (0.82, 0.41), co-substitution of Co and Te does not further increase the *ZT* values with respect to samples solely substituted with either Co or Te.

Acknowledgements

The authors thank S. Mathieu for providing experimental support in the EDXS/WDXS measurements.

References

1 *Thermoelectrics and its Energy Harvesting*, ed. D. M. Rowe, CRC Press, 2012.

2 H. J. Goldsmid, in *Thermoelectric Refrigeration*, Temple Press Books, Ltd., London, 1964.

3 G. J. Snyder and E. S. Toberer, *Nat. Mater.*, 2008, **7**, 105-114.

4 J. R. Sootsman, D. Y. Chung and M. G. Kanatzidis, *Angew. Chem. Int. Ed.*, 2009, **48**, 8616–8639.

5 K. Suekuni, F. S. Kim and T. Takabatake, *J. Appl. Phys.*, 2014, **116**, 063706.

6 K. Suekuni, F. S. Kim, H. Nishiate, M. Ohta, H. I. Tanaka and T. Takabatake, *Appl. Phys. Lett.*, 2014, 105, 132107.

7 P. Qiu, T. Zhang, Y. Qiu, X. Shi and L. Chen, *Energy Environ. Sci.*, 2014, **7**, 4000-4006.

8 G. Guélou, A. V. Powell and P. Vaqueiro, *J. Mater. Chem. C*, 2015, **3**, 10624-10629.

9 C. Bourgès, P. Lemoine, O. I. Lebedev, R. Daou, V. Hardy, B. Malaman and E. Guilmeau, *Acta Mater.*, 2015, **97**, 180-190.

10 K. Suekuni, K. Tsuruta, T. Ariga and M. Koyano, *Appl. Phys. Express*, 2012, **5**, 051201.

11 X. Lu, D. T. Morelli, Y. Xia, F. Zhou, V. Ozolins, H. Chi, X. Zhou and C. Uher, *Adv. Energy Mater.*, 2013, **3**, 342-348.

12 X. Lu and D. T. Morelli, *Phys. Chem. Chem. Phys.*, 2013, **15**, 5762-5766.

13 K. Suekuni, K. Tsuruta, M. Kunii, H. Nishiate, E. Nishibori, S. Maki, M. Ohta, A. Yamamoto and M. Koyano, *J. Appl. Phys.*, 2013, **113**, 043712.

14 J. Heo, G. Laurita, S. Muir, M. A. Subramanian and D.A. Keszler, *Chem. Mater.*, 2014, **26**, 2047-2052.

15 R. Chetty, D. S. Prem Kumar, G. Rogl, P. Rogl, E. Bauer, H. Michor, S. Suwas, S. Puchegger, G. Giester and R. C. Mallik, *Phys. Chem. Chem. Phys.*, 2015, **17**, 1716-1727.

16 T. Barbier, P. Lemoine, S. Gascoin, O. I. Lebedev, A. Kaltzoglou, P. Vaqueiro, A. V.

Powell, R.I. Smith and E. Guilmeau, J. Alloys Compd., 2015, **634**, 253-262.

17 Y. Bouyrie, C. Candolfi, S. Pailhès, M. M. Koza, B. Malaman, A. Dauscher, J. Tobola, O. Boisron, L. Saviot and B. Lenoir, *Phys. Chem. Chem. Phys.*, 2015, **17**, 19751-19758.

18 E. Lara-Curzio, A. F. May, O. Delaire, M. A. McGuire, X. Lu, C.-Y. Liu, E. D. Case and D. T. Morelli, *J. Appl. Phys.*, 2014, **115**, 193515.

19 R. Chetty, A. Bali, M. H. Naik, G. Rogl, P. Rogl, M. Jain, S. Suwas and R. C. Mallik, *Acta Mater.*, 2015, **100**, 266-274.

20 W. Lai, Y. Wang, D. T. Morelli and X. Lu, *Adv. Funct. Mater.*, 2015, **25**, 3648-3657.

21 Y. Bouyrie, C. Candolfi, V. Ohorodniichuk, B. Malaman, A. Dauscher, J. Tobola and B. Lenoir, *J. Mater. Chem. C*, 2015, **3**, 10476-10487.

22 X. Lu and D. T. Morelli, *J. Elec. Mater.*, 2014, **43**, 1983.

23 X. Lu, D. T. Morelli, Y. Xia and V. Ozolins, *Chem. Mater.*, 2015, **27**, 408-413.

24 Y. Bouyrie, C. Candolfi, J.-B. Vaney, A. Dauscher and B. Lenoir, *J. Elec. Mater.* DOI: 10.1007/s11664-015-4128-3.

25 J. Rodriguez-Carvajal, *Physica B*, 1993, 192, 55-69.

26 E. Alleno, D. Bérardan, C. Byl, C. Candolfi, R. Daou, R. Decourt, E. Guilmeau, S. Hébert, J. Hejtmanek, B. Lenoir, P. Masschelein, V. Ohorodniichuk, M. Pollet, S. Populoh, D. Ravot, O. Rouleau and M. Soulier, *Rev. Sci. Instrum.*, 2015, **86**, 011301.

27 M. L. Johnson and R. Jeanloz, *Am. Mineral.*, 1983, **68**, 220-226.

28 B. J. Skinner, F. D. Luce and E. Makovicky, *Econ. Geol.*, 1972, 67, 924-938.

29 E. Makovicky and B. J. Skinner, *Can. Mineral.*, 1978, **16**, 611-623.

30 K. Tatsuka and N. Morimoto, *Am. Mineral.*, 1973, **58**, 425-434.

31 K. Tatsuka and N. Morimoto, *Econ. Geol.*, 1977, **72**, 258-270.

32 Y. Bouyrie, C. Candolfi, A. Dauscher, B. Malaman and B. Lenoir, *Chem. Mater.*, 2015, **27**, 8354.

33 K. Kurosaki, A. Kosuga, H. Muta, M. Uno and S. Yamanaka, *Appl. Phys. Lett.*, 2005, **87**, 061919.

34 D. C. Schmitt, N. Haldolaarachchige, Y. Xiong, D. P. Young, R. Jin and J. Y. Chan, *J. Am. Chem. Soc.*, 2014, **134**, 5965−5973.

35 Q. Guo, M. Chan, B. A. Kuropatwa and H. Kleinke, *Chem. Mater.*, 2013, **25**, 4097−4104.

36 Q. Guo, A. Assoud and H. Kleinke, Adv. Energy Mater., 2014, **4**, 1400348.

37 P. Gougeon, P. Gall, R. Al Rahal Al Orabi, B. Fontaine, R. Gautier, M. Potel, T. Zhou, B. Lenoir, M. Colin, C. Candolfi and A. Dauscher, *Chem. Mater.*, 2012, **24**, 2899−2908.

38 R. Al Rahal Al Orabi, P. Gougeon, P. Gall, B. Fontaine, R. Gautier, M. Colin, C. Candolfi, A. Dauscher, J. Hejtmanek, B. Malaman and B. Lenoir, *Inorg. Chem.*, 2014, **53**, 11699−11709.

39 S. R. Brown, S. M. Kauzlarich, F. Gascoin and G. J. Snyder, *Chem. Mater.*, 2006, **18**, 1873−1877.

40 S. K. Bux, A. Zevalkink, O. Janka, D. Uhl, S. M. Kauzlarich, G. J. Snyder and J.-P. Fleurial, *J. Mater. Chem. A*, 2014, **2**, 215−220.

41 D. G. Cahill, S. K. Watson and R. O. Pohl, *Phys. Rev. B: Condens. Matter Mater. Phys.*, 1992, **46**, 6131.

Table Captions

Table 1. Nominal and actual compositions measured by EDXS/WDXS for $Cu_{12-x}Co_xSb_4S_{13}$ and $Cu_{12-x}Co_xSb_{4-y}Te_yS_{13}$. The chemical formulae were normalized to 13 sulfur atoms per formula unit.

Series Co		*Series Co-Te*	
Nominal composition	*Actual composition*	*Nominal composition*	*Actual composition*
$Cu_{11.00}Co_{1.00}Sb_4S_{13}$	$Cu_{11.62}Co_{0.90}Sb_{4.16}S_{13}$	$Cu_{11.5}Co_{0.5}Sb_{3.5}Te_{0.5}S_{13}$	$Cu_{12.18}Co_{0.25}Sb_{3.68}Te_{0.62}S_{13}$
$Cu_{10.75}Co_{1.25}Sb_4S_{13}$	$Cu_{10.96}Co_{1.30}Sb_{3.83}S_{13}$	$Cu_{11.5}Co_{0.5}Sb_{3.25}Te_{0.75}S_{13}$	$Cu_{11.67}Co_{0.47}Sb_{3.36}Te_{0.77}S_{13}$
$Cu_{10.50}Co_{1.50}Sb_4S_{13}$	$Cu_{10.73}Co_{1.51}Sb_{4.07}S_{13}$	$Cu_{11.5}Co_{0.5}Sb_3Te_1S_{13}$	$Cu_{11.88}Co_{0.32}Sb_{3.11}Te_{1.05}S_{13}$
$Cu_{10.25}Co_{1.75}Sb_4S_{13}$	$Cu_{10.48}Co_{1.70}Sb_{4.01}S_{13}$	$Cu_{11.0}Co_{1.0}Sb_{2.5}Te_{0.5}S_{13}$	$Cu_{11.47}Co_{0.82}Sb_{3.78}Te_{0.41}S_{13}$

Table 2. Lattice parameters *a* of the $Cu_{12-x}Co_xSb_4S_{13}$ and $Cu_{12-x}Co_xSb_{4-y}Te_yS_{13}$ samples determined by Rietveld refinements against the PXRD patterns. The lattice parameters of the Co-Te series are compared to those expected by considering the Co and Te concentrations measured by EDXS/WDXS and by using the linear variations of *a* with *x* and *y* determined in the $Cu_{12-x}Co_xSb_4S_{13}$ and $Cu_{12}Sb_{4-y}Te_yS_{13}$ tetrahedrites (Ref. 19 and 21).

Series Co		*Series Co-Te*		
x	*a (Å)*	*(x,y)*	*a (Å)*	*a (Å) expected*
0.90	10.3300(2)	(0.25, 0.62)	10.3324(2)	10.3323
1.30	10.3337(2)	(0.47, 0.77)	10.3383(2)	10.3382
1.51	10.3369(2)	(0.32, 1.05)	10.3410(2)	10.3435
1.70	10.3399(2)	(0.82, 0.41)	10.3389(2)	10.3385

Figure Captions

Figure 1. Rietveld refinements of one illustrative samples of each series: (a) $Cu_{10.48}Co_{1.70}Sb_{4.01}S_{13}$ and (b) $Cu_{12.18}Co_{0.25}Sb_{3.68}Te_{0.62}S_{13}$. The asterisk in panel (a) marks the impurity phase identified as $CuSbS_2$. The experimental data are marked as red dots, the calculated pattern is in black and the difference between experimental and calculated patterns is shown in blue. The vertical green bars stand for the expected Bragg positions of the cubic crystal lattice of tetrahedrites.

Figure 2. Backscattered electron (BSE) image and corresponding X-ray elemental maps of the x = 1.70 sample showing the good chemical homogeneity of the matrix (a) despite the presence of minute amounts of secondary phases identified as $CuSbS_2$ and CoS_2 (b). The scale bars correspond to 10 and 50 μm in panels (a) and (b), respectively.

Figure 3. Secondary electron (SE) image and X-ray maps of the co-substituted (x,y) = (0.82, 0.41) sample. The scale bar corresponds to 30 μm.

Figure 4. Lattice parameter a as a function of x and $x + y$ for the Co (a) and Co-Te (b) series, respectively. The solid black lines are guides to the eye.

Figure 5. Temperature dependence of the electrical resistivity ρ of the (a) $Cu_{12-x}Co_xSb_4S_{13}$ and (b) $Cu_{12-x}Co_xSb_{4-y}Te_yS_{13}$ tetrahedrites.

Figure 6. Thermopower α as a function of the temperature for the (a) $Cu_{12-x}Co_xSb_4S_{13}$ and (b) $Cu_{12-x}Co_xSb_{4-y}Te_yS_{13}$ samples.

Figure 7. Total thermal conductivity κ as a function of the temperature for the series (a) $Cu_{12-x}Co_xSb_4S_{13}$ and (b) $Cu_{12-x}Co_xSb_{4-y}Te_yS_{13}$. The difference observed between the low-temperature and high-temperature data sets near room temperature is due to thermal radiations that obscure the intrinsic κ values. The lattice thermal conductivity κ_L of the $Cu_{12-x}Co_xSb_4S_{13}$ (c) and $Cu_{12-x}Co_xSb_{4-y}Te_yS_{13}$ (d) series has been estimated by considering degeneracy-adjusted Lorenz numbers.

Figure 8. Temperature dependence of the dimensionless thermoelectric figure of merit *ZT* for the (a) $Cu_{12-x}Co_xSb_4S_{13}$ and (b) $Cu_{12-x}Co_xSb_{4-y}Te_yS_{13}$ samples.

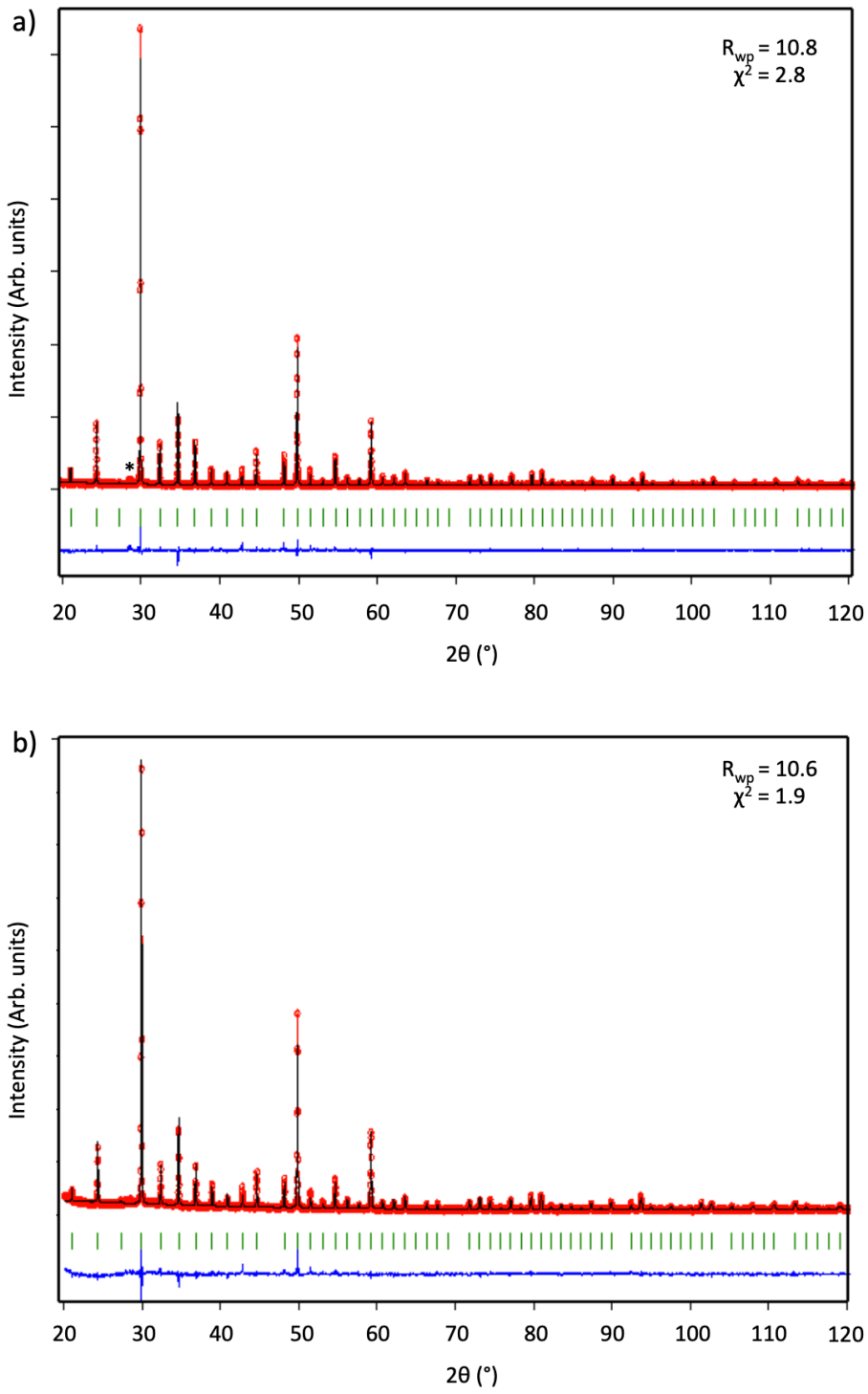
a)
R_{wp} = 10.8
χ^2 = 2.8
Intensity (Arb. units)
*
20
30
40
50
60
70
80
90
100
110
120
2θ (°)
b)
R_{wp} = 10.6
χ^2 = 1.9
Intensity (Arb. units)
20
30
40
50
60
70
80
90
100
110
120
2θ (°)

Figure 1

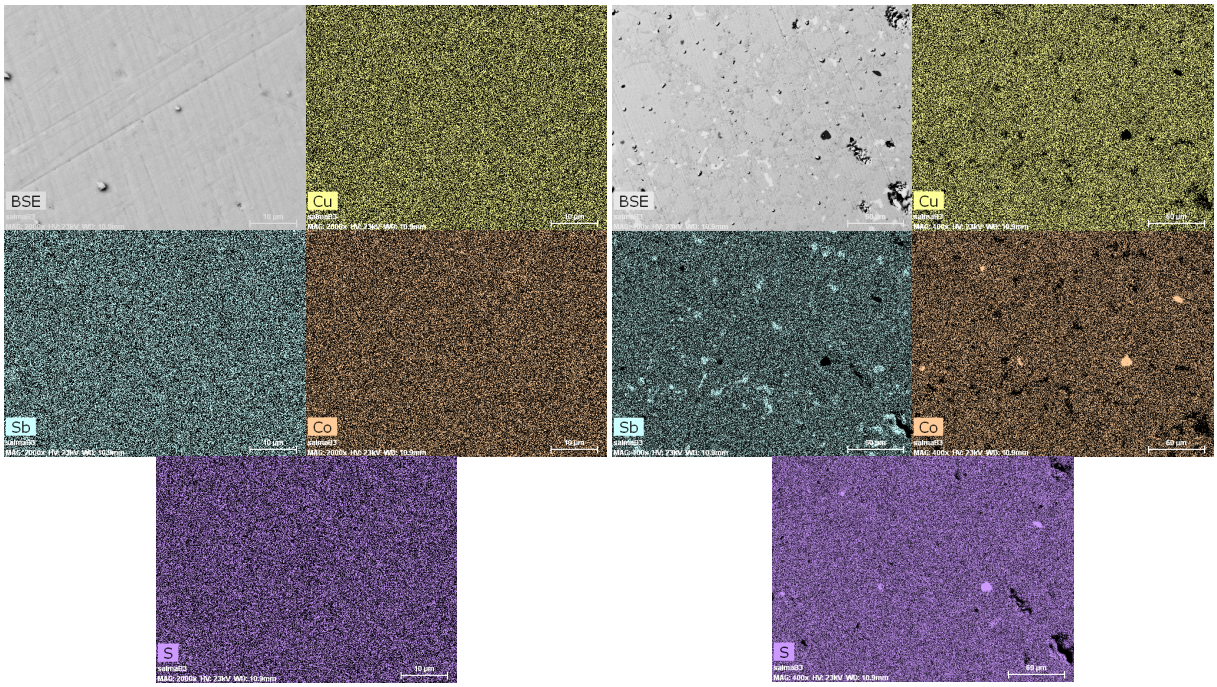

a) b)

Figure 2

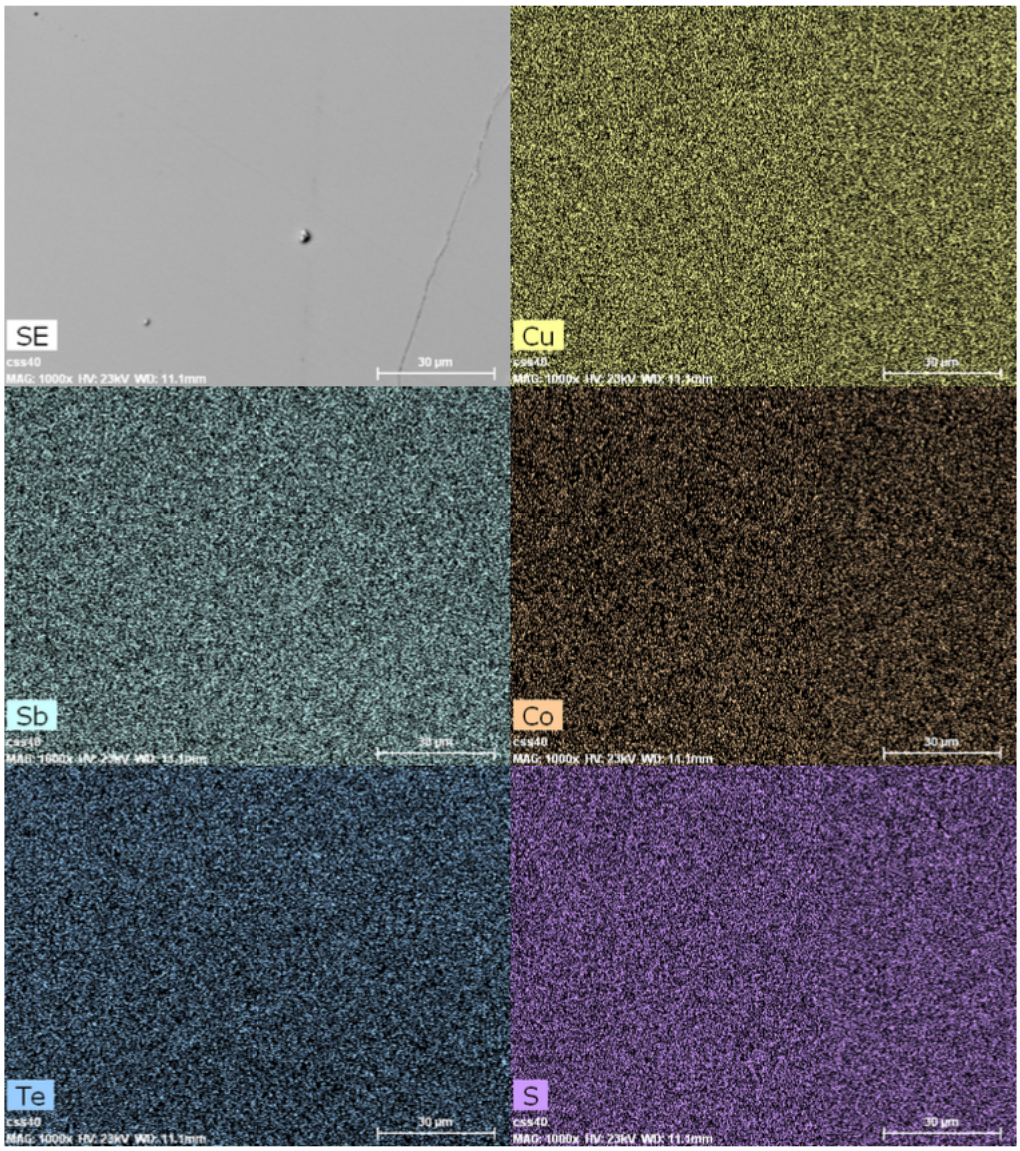

Figure 3

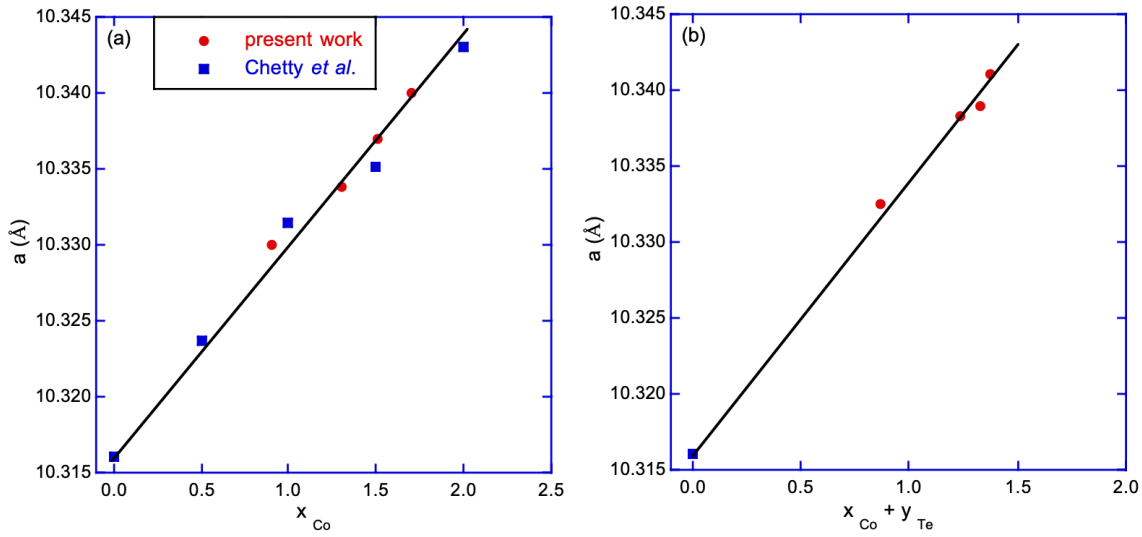

Figure 4

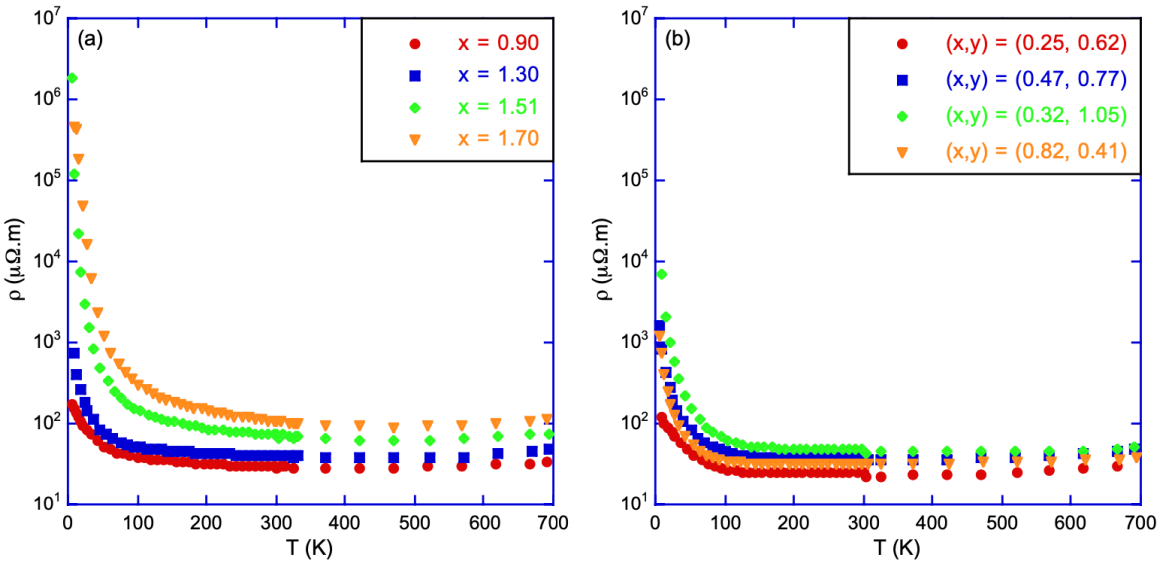
(a)
x = 0.90
x = 1.30
x = 1.51
x = 1.70
ρ (μΩ.m)
T (K)
(b)
(x,y) = (0.25, 0.62)
(x,y) = (0.47, 0.77)
(x,y) = (0.32, 1.05)
(x,y) = (0.82, 0.41)
ρ (μΩ.m)
T (K)

Figure 5

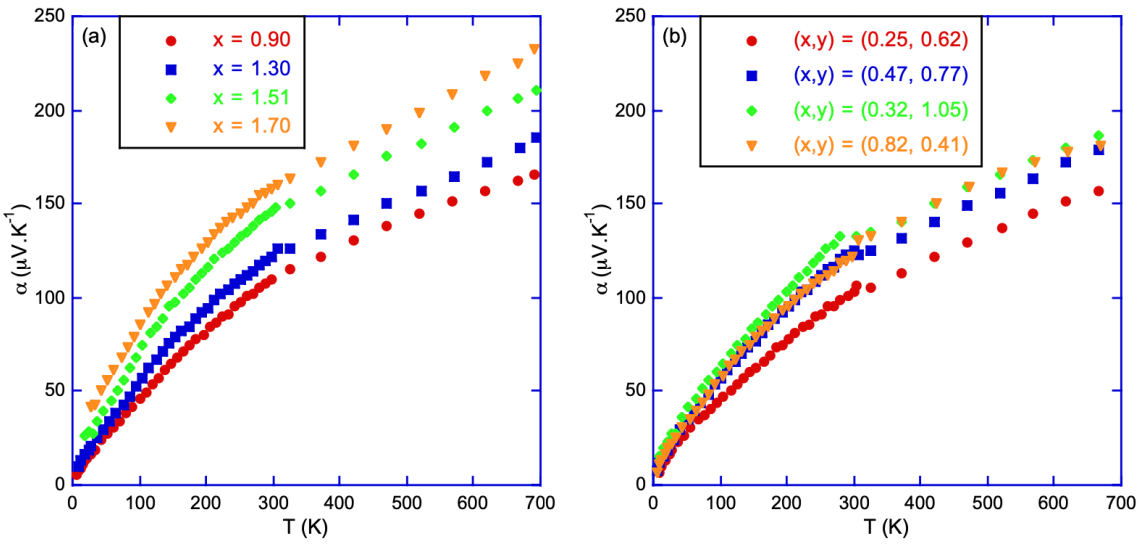
(a)
x = 0.90
x = 1.30
x = 1.51
x = 1.70
α (μV.K-1)
T (K)
(b)
(x,y) = (0.25, 0.62)
(x,y) = (0.47, 0.77)
(x,y) = (0.32, 1.05)
(x,y) = (0.82, 0.41)
α (μV.K-1)
T (K)

Figure 6

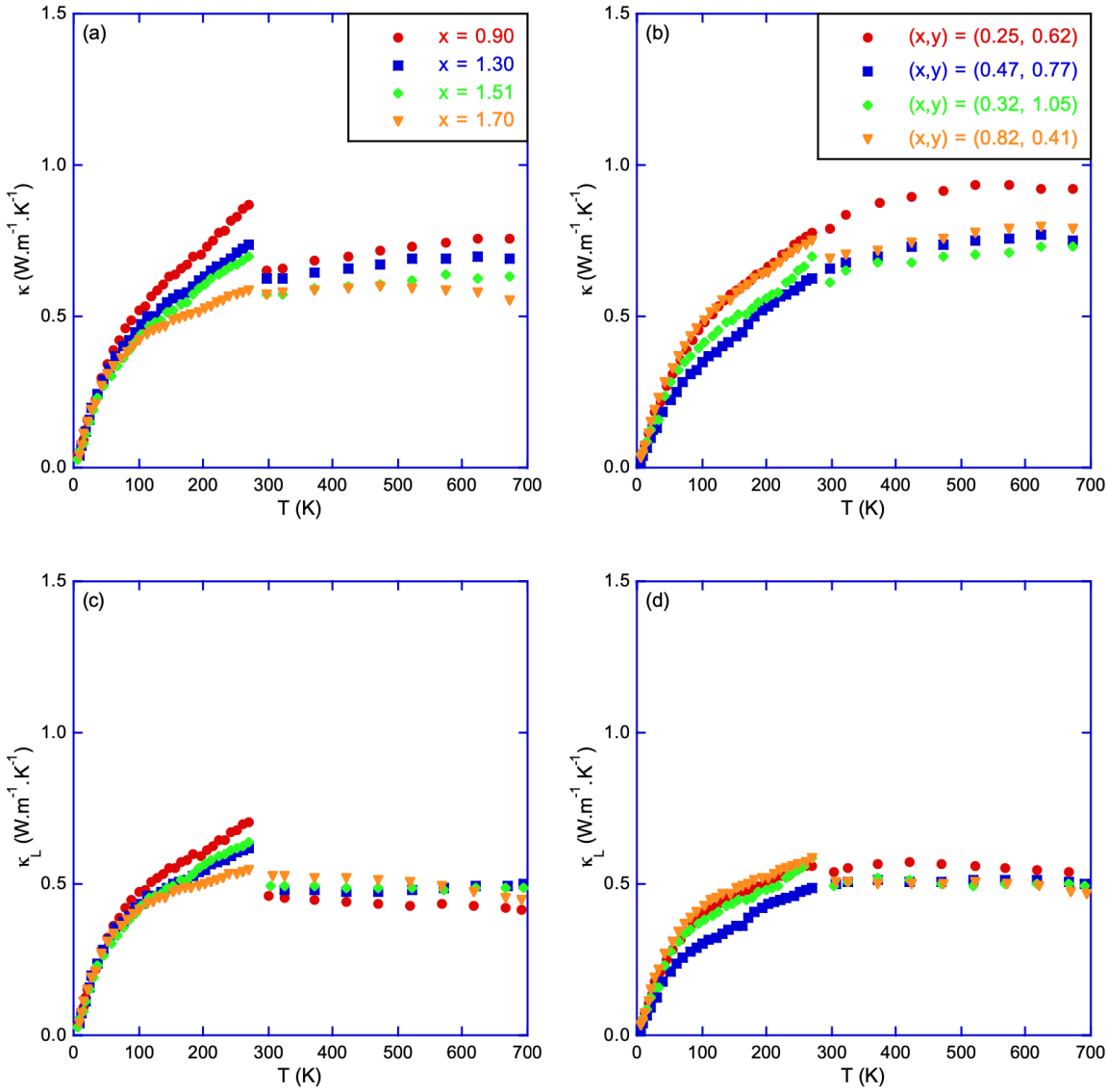
(a)
x = 0.90
x = 1.30
x = 1.51
x = 1.70
κ (W.m-1.K-1)
T (K)
(b)
(x,y) = (0.25, 0.62)
(x,y) = (0.47, 0.77)
(x,y) = (0.32, 1.05)
(x,y) = (0.82, 0.41)
κ (W.m-1.K-1)
T (K)
(c)
κL (W.m-1.K-1)
T (K)
(d)
κL (W.m-1.K-1)
T (K)

Figure 7

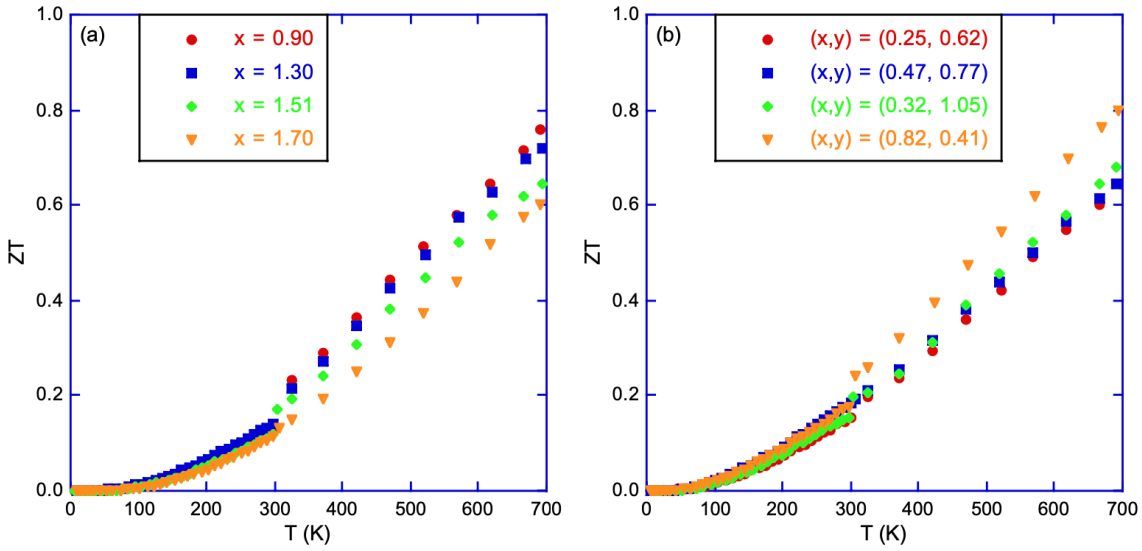
(a)
x = 0.90
x = 1.30
x = 1.51
x = 1.70
ZT
T (K)
(b)
(x,y) = (0.25, 0.62)
(x,y) = (0.47, 0.77)
(x,y) = (0.32, 1.05)
(x,y) = (0.82, 0.41)
ZT
T (K)

Figure 8